



Effect of die misalignment on the joining quality of Al/steel self-piercing riveting structure

Yuxuan Liao¹ · Jun Zhang¹ · Gusheng Wu² · Guangyao Li^{1,3} · Junjia Cui¹ · Hao Jiang¹

Received: 9 October 2023 / Accepted: 19 December 2023 / Published online: 15 January 2024
© The Author(s), under exclusive licence to Springer-Verlag France SAS, part of Springer Nature 2024

Abstract

Self-piercing riveting (SPR) is one of the advanced mechanical joining techniques, and it has been widely used in automobile industry. In this paper, the effect of die misalignment on the cross-section parameters and mechanical properties of SPR joints were respectively studied through numerical simulation and experiment, and the mechanical properties degradation mechanism of the misaligned riveted joint were analyzed. A three-dimensional explicit finite element model (FEM) of SPR joint was developed by ABAQUS, and the section observation was performed to evaluate the accuracy of FEM. The riveting process and the strain of SPR joints with different misalignment distance was analyzed, and the quasi-static shear test was carried out. The results revealed that the rivet leg near the die edge was thickened due to limitations in deformation space, and a cavity was formed at the outer edge of the rivet leg near the die center, during the riveting process. It resulted in different cross-section parameters and mechanical properties of SPR joints. Specifically, the interlock distance decreased as the misalignment distance increased. The bottom thickness of the side near the die edge increased with increasing misalignment distance, while that near the die center decreased slightly as the misalignment distance increased. In addition, the maximum shear load decreased nonlinearly with increasing misalignment distance, and the movement of die along the loading end had a significantly greater impact on the maximum shear load than the movement along the fixed end. This was mainly because the interlock distance of SPR joints was asymmetrically and nonlinearly reduced due to the die misalignment.

Keywords Self-piercing riveting · Die misalignment · Numerical simulation · Cross-section parameters · Mechanical properties

Introduction

Nowadays, the use of lightweight materials is one of the important means to reduce the weight of vehicle [1]. Replacing traditional steel material with lightweight aluminum alloys has become a common trend in the automotive industry [2]. It allows the connection of dissimilar materials. Self-piercing riveting (SPR) originated half a century ago, but it has developed significantly in the past 25 years due to the requirements of the automotive industry for joining

lightweight structures, such as aluminum alloy structures, aluminum-steel structures and other mixed-material structures [3]. SPR is one of the advanced mechanical joining techniques that provides a viable alternative to spot welding [4]. It has been widely used by automotive manufacturers because of the advantages, such as no pre-drilling, high joint strength and stiffness, environmental friendliness and automatic application [5].

At present, some researchers have demonstrated that SPR joints have excellent performance in some aspects compared to spot welded joints. Han et al. [6] demonstrated that SPR joints generally achieve similar or higher peel strengths than the resistance spot welded (RSW) joints with aluminum sheets in the automotive industry, and the performance of SPR joints improves with increasing thickness. Asati et al. [7] also found the fatigue performance of SPR joints was significantly superior to those of RSW joints. In addition, many researchers have studied the influence of process parameters on the mechanical properties of SPR joint. Deng et al. [8]

✉ Hao Jiang
haojiang@hnu.edu.cn

¹ State Key Laboratory of Advanced Design and Manufacturing Technology for Vehicle, Hunan University, Changsha 410082, China

² Hunan Yufeng Fasteners Co., Ltd, Changsha 410082, China

³ Shenzhen Automotive Research Institute, Beijing Institute of Technology, Shenzhen 518118, China

investigated the effect of variation in die geometry on the peak load and energy absorption of the joints, such as the die groove shape, cone height, and die radius. Research has found that the joints with a single conical-section die exhibit higher tensile strength and energy absorption compared to those with a double conical-section die. It is because the die design parameters significantly influence the plastic flow of materials and the change in cross-section of SPR joints, as indicated by Karathanasopoulos et al. [9]. Jiang et al. [10] conducted a series of tests to explore the effects of the geometrical parameters of rivets on the electromagnetic SPR process such as blade angles, inner diameters and leg lengths. And they obtained the rivet suitable for electromagnetic SPR. Karim et al. [11] also indicated the rivet coatings have an impact on the joint quality and strength of SPR joints. Specifically, the SPR joint with Zn-Ni-coated rivets exhibit deeper rivet head penetration and greater interlocking owing to the lower friction coefficient. Moreover, Duan et al. [12] showed the maximum shear load, absorbed energy and deformation resistance decreased as the distance from the riveting point to the sheets edge decreased. Chen et al. [13] also indicated the interaction of sheet thickness and rivet hardness has the greatest impact on the maximum riveting force and failure load of SPR joints.

However, the experimental study of SPR joints has been proven to be a time-consuming and expensive task. Replacing experiments with detailed simulation models is expected to be an effective solution to shorten the research cycle [14]. Du et al. [15] constructed a 2D axisymmetric numerical model based on r-adaptivity method to simulate the SPR process. The results indicated that the undercut decreases with the increase of sheet flow stress ratio, while the opposite trend is observed for the minimum thickness. Zhao et al. [16] investigated systematically the influences of the sheet thickness and rivet length on the formation mechanisms of SPR joint by combining experimental tests with a finite element model (FEM). In addition, Lin et al. [17] proposed a prediction method of the cross-tension strength of SPR joints on the basis of FEM and extreme gradient boosting decision tree algorithm. Rusia et al. [4] also proposed an end-to-end simulation process chain for predicting the geometry and strength of SPR joints. All the above studies were aimed at studying the cross-sectional parameters and mechanical properties of normal riveted joints.

In order to establish a more comprehensive and reliable process research, the relevant studies of joint defects are also a very important part, in addition to conducting relevant studies on the process parameters and mechanical properties of SPR joint. The die misalignment is a common SPR joint defect. During the SPR process, the manufacturing errors of the rivet, rivet gun and die, as well as the assembly errors of the rivet gun and die, cause the axes of the rivet and die to be non-concentric, resulting in the die misalignment [18].

However, the effect of die misalignment on the connection quality of SPR joint has not been systematically studied.

In this paper, the effect of die misalignment on the joining quality of SPR joints was investigated by numerical simulation and experimental study. First, a three-dimensional explicit FEM of the SPR joint was developed by ABAQUS. Then, the section observation was performed to evaluate the accuracy of FEM. Finally, the effects of die misalignment on the cross-section parameters and mechanical properties of SPR joints were respectively studied through numerical simulation and experiment, and the mechanical properties degradation mechanism of the misaligned riveted joint were analyzed.

Experimental materials and methods

Specimen preparation

In this study, 5052 aluminum alloy (AA5052) sheets and DP590 high strength steel sheets are riveted by the self-piercing riveting machine (IRIVET-ZCM-8 L), as shown in Fig. 1a. The size of AA5052 and DP590 sheets is determined as 120.0×40.0 mm, and the thicknesses is 2.0 mm. All sheets are cut along the rolling direction, and the overlapping length is 40.0 mm. The steel sheet is placed on the side of the riveting die for better joint forming [19], as shown in Fig. 1b. The fasteners are P-SK 5*6 semi-hollow rivets made of 45# carbon steel (ASTM 1045) and manufactured by Böllhoff Co. The hardness state of rivets was H4 (44 ± 2 HRC). The die was supplied by the manufacturer based on the connecting material and sheet thickness. The specific dimensions of the rivet and die are shown in Fig. 1c and d, respectively. The mechanical properties and elementary compositions of the sheets and rivets are listed in Table 1.

The misaligned riveted joint is characterized by a non-concentric circle on the bottom sheets, as shown in Fig. 2. In this study, the degree of die misalignment was controlled by the offset distance of the die relative to the rivet. And 11 sets of test specimens were produced, as shown in Table 2.

Section observations and mechanical property tests

The connection mechanism of SPR joint is the formation of mechanical interlocking structure due to the plastic deformation of the connected sheets and rivet during the rivet pressing process [20]. Therefore, the cross-section parameters have an important influence on the quality of SPR joints. At present, the joint quality is generally evaluated by the cross-sectional observation [21]. Figure 3 shows the schematic of the three general evaluating indicators for SPR joints: the residual height of rivet head (H), the interlock distance between sheets and rivets (I) and the bottom thickness of

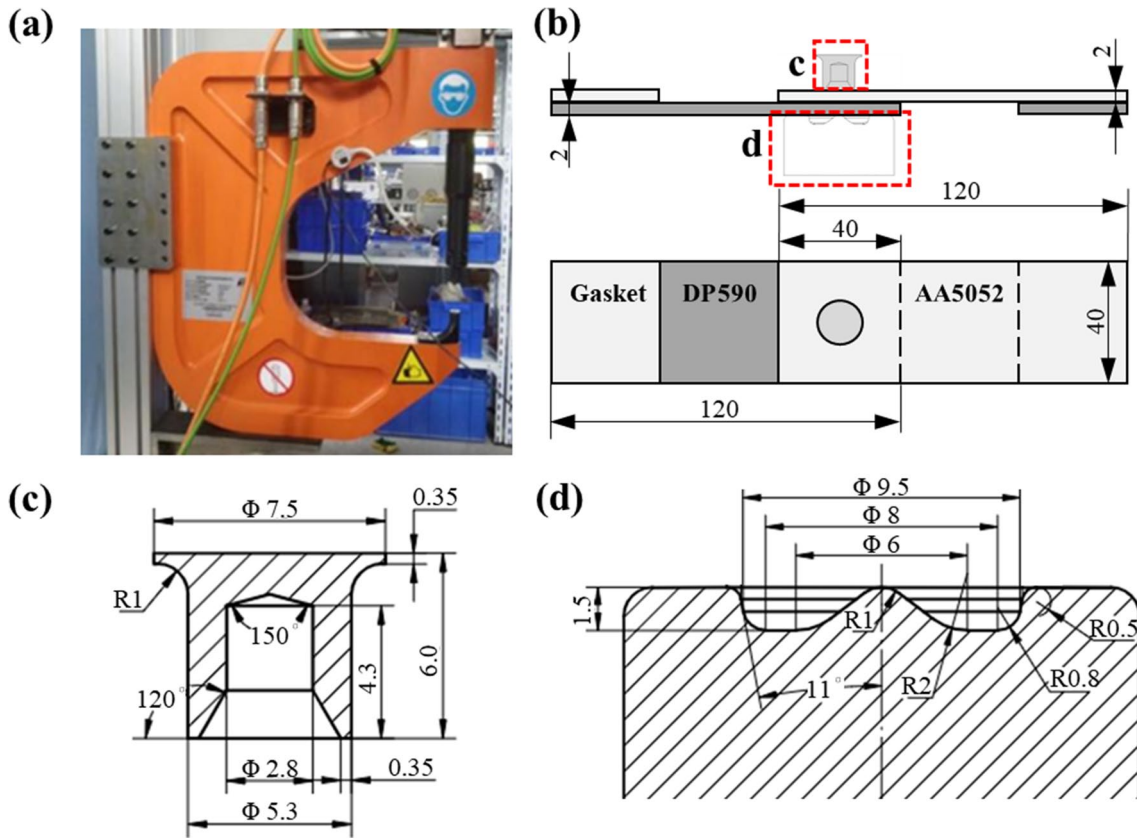


Fig. 1 Specimen preparation: **a** the self-piercing riveting machine; **b** the schematic of the riveted specimens; the specific dimensions of **(c)** the rivet and **(d)** the die (dimensions in mm)

Table 1 The mechanical properties and elementary compositions of sheets and rivets

Properties	Materials		
	AA5052 sheet	DP590 sheet	45# steel rivet
Density (g/cm ³)	2.68	7.85	7.85
Yield strength(MPa)	148	379	412
Tensile strength(MPa)	212	626	684
Tensile modulus (GPa)	70	208	210
Poisson ratio	0.33	0.33	0.3
Elementary compositions(wt%)	Si=0.14, Fe=0.36, Cu=0.01, Mn=0.05, Mg=2.48, Cr=0.17, Al=balance	C=0.095, Si=0.16, Mn=1.9; Mo=0.09, S=0.004, Fe=balance	C=0.45, Cr=0.20, Mn=0.55, Si=0.28, Ni=0.20, S=0.01, Fe=balance

joint (T). Specifically, H indicates the height of the rivet head relative to the surface of top sheet after riveting. I represents the offset distance between outer surface of rivet shank tip and the point where the rivet pierces through the upper sheet. The parameter reflects the degree of interlock between the rivet and sheets, and directly influences the mechanical properties of SPR joints [22]. T represents the

distance from the tip of rivet leg to the surface of bottom sheet. It is necessary to keep a suitable bottom thickness to ensure that the rivets do not penetrate the bottom sheet [23]. In addition, the rivet head diameter (D) has been added as the control parameter to determine whether to cut and polish along the center of SPR joints. In this study, the SPR joints firstly were cut along the center using a multi-functional

Fig. 2 The schematic of SPR joint: **a** the normal riveted joint; **b** the misaligned riveted joint

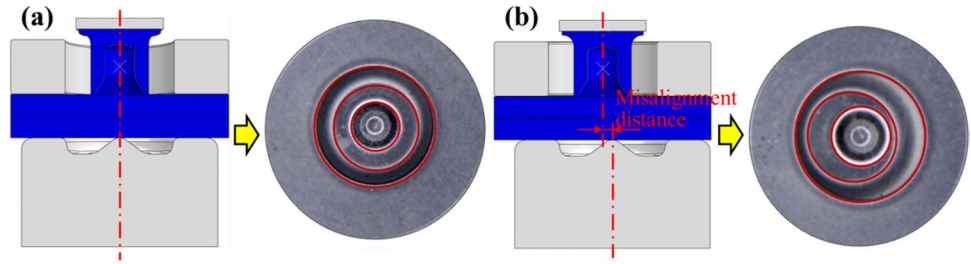


Table 2 The misalignment distance of test specimens

No.	0	1	2	3	4	5	6	7	8	9	10
Misalignment distance (mm)	0	0.1	0.2	0.3	0.4	0.5	0.6	0.7	0.8	0.9	1.0

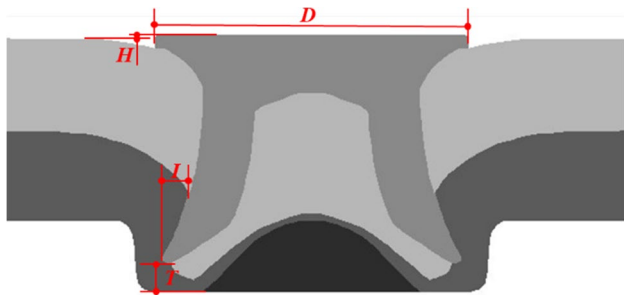


Fig. 3 The cross-section parameters of SPR joints

CNC wire cutting machine, and then mechanically polished by a metallographic polishing instrument. Finally, the cross-section parameters were observed and measured by Olympus OLS4100-SAF confocal laser microscope.

Quasi-static shear test was carried out by Instron 5985 universal testing machine, as shown in Fig. 4. The tensile test speed was set as 2 mm/min. Three repeated tensile tests were conducted to obtain the shear load–displacement curves and the maximum shear loads for the specimens. In addition, all specimens were fitted with the metal gaskets of the same thickness as the sheets in order to prevent the specimens from bending during shear tests [24].

Numerical simulation model

In this study, a three-dimensional explicit FEM of the SPR joint was developed by ABAQUS, as shown in Fig. 5a. The model was composed of six components: the punch (providing pressure), the rivet (piercing the top sheet to complete the self-locking connection), the blank holder (preventing the top sheet from slipping and warping), the top and bottom

Fig. 4 The quasi-static shear test

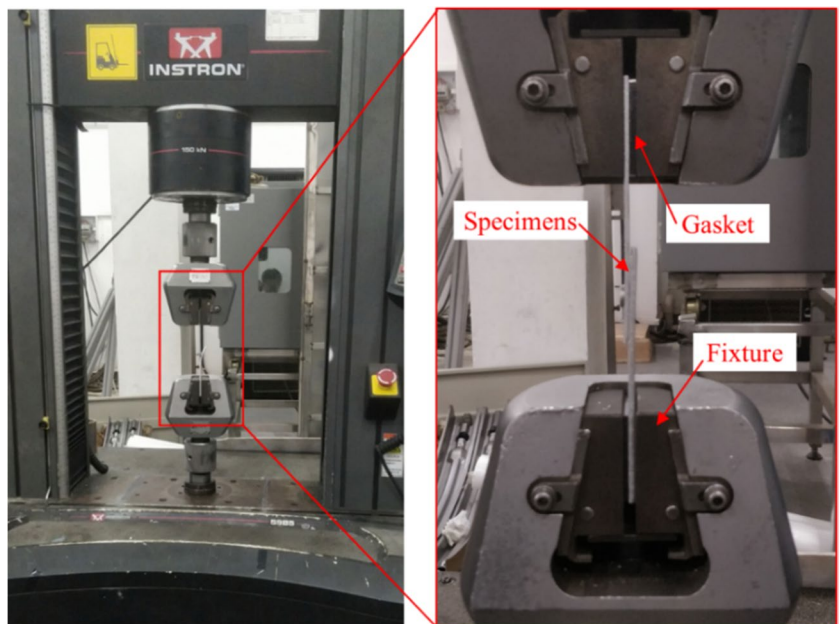
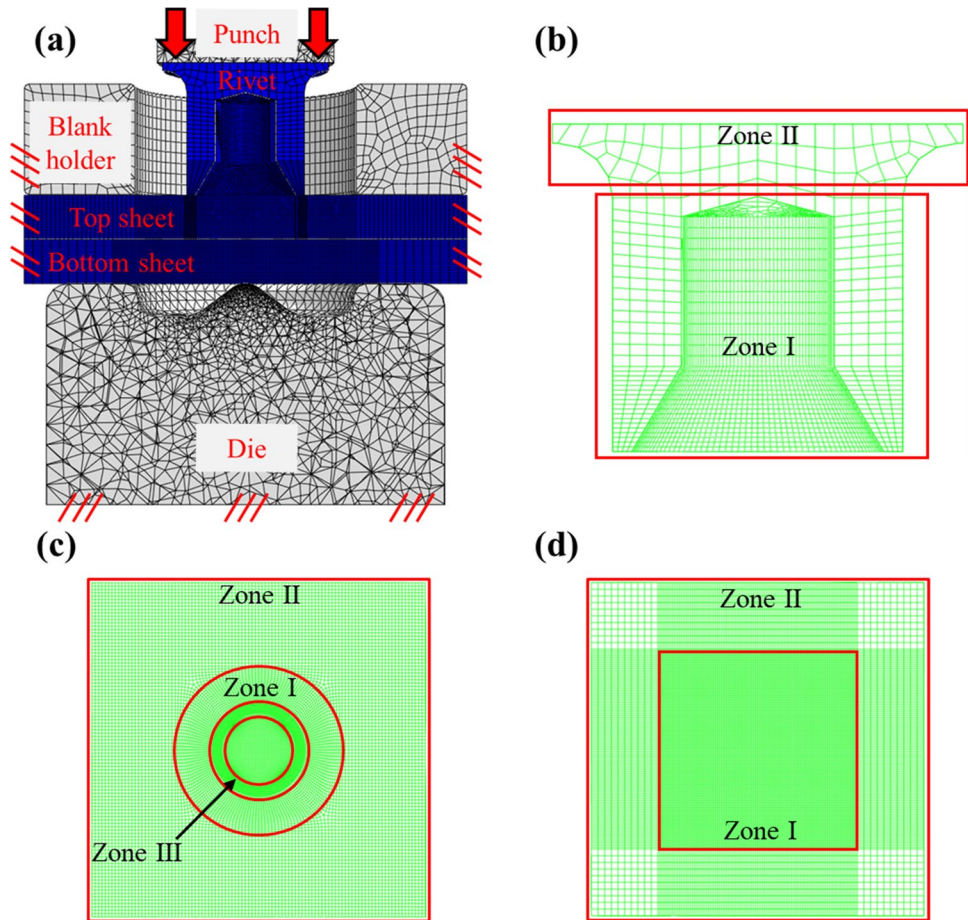


Fig. 5 The establishment of numerical simulation model: (a) the three-dimensional explicit FEM of SPR joint; the mesh of (b) rivet, (c) top sheet, and (d) bottom sheet



sheets (2 mm thickness), and the die (limiting the deformation of the rivet and bottom sheet). Among them, the blank holder, the die and the edge of the sheets were set as fixed elements (no displacement and rotation). The punch could not rotate and only moved in the vertical direction. In this study, the riveting process was simulated by controlling the displacement of punch. The stroke distance was set to 6 mm, which was the same as the length of rivets.

The main components involved in deformation were the rivet, top and bottom sheets. The rivet and sheets were both segmented in the model to refine the mesh. Specifically, the mesh density of the rivet legs was large due to the major deformation (zone I), while the mesh density of the nail head was less due to the minor deformation (zone II), as shown in Fig. 5b. During the riveting process, the fracture failure would occur in the top sheet. The mesh quality of the top sheet greatly affected the simulation results. Therefore, the top sheet was divided into three zones and assigned different mesh densities, as shown in Fig. 5c. The circular area inside the blank holder was the major deformation zone I, and the other areas was the minor deformation zone II. The ring area under the rivet leg was the failure zone III. In addition, only deformation

occurred on the bottom sheet during the riveting process, and no fracture occurred. The bottom sheet was divided into two zones and assigned different mesh densities: the major deformation zone I and the minor deformation zone II, as shown in Fig. 5d. Furthermore, the rest of the components (i.e., punch, blank holder and die) were regarded as rigid objects.

During the riveting process, local plastic deformation occurred around the major deformation zone I of the top sheet and bottom sheet, resulting in some mechanical energy being converted into heat. Considering the effects of work hardening, strain rate and thermal softening, the *J-C* constitutive equation was used to establish the constitutive relation of the metal materials studied in this paper [25]. Its expression was:

$$\sigma = [A + B\varepsilon^n][1 + C \ln \frac{\dot{\varepsilon}}{\dot{\varepsilon}_0}][1 - \left(\frac{T - T_r}{T_m - T_r}\right)^m] \quad (1)$$

where σ is the stress; ε is the plastic strain; $\dot{\varepsilon}$ and $\dot{\varepsilon}_0$ represent respectively the experimental strain rate and the reference strain rate; A , B , C , n and m represent respectively the yield stress parameter, hardening factor, strain rate factor,

Table 3 *J-C* material model parameters of the sheets

Materials	A	B	C	<i>n</i>	<i>m</i>	$\dot{\epsilon}_0(s^{-1})$
DP590	392	697	0.0153	0.4	—	0.02
Al5052	143.1	251.7	0.0046	0.44	0.9	0.01

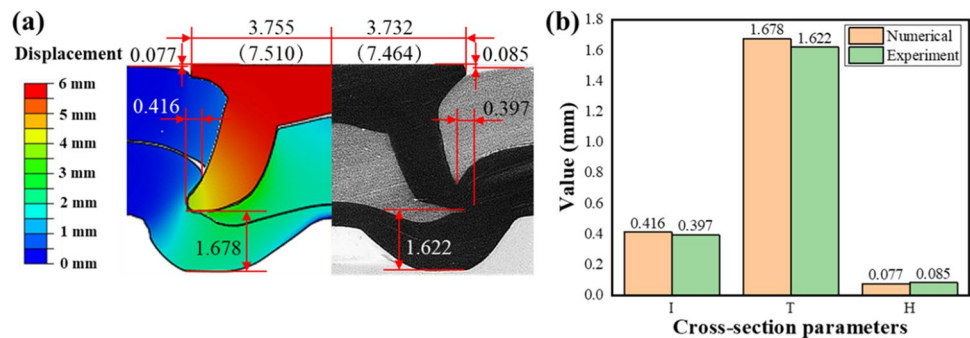
Table 4 *J-C* failure model parameters of the sheets

Materials	<i>d</i> ₁	<i>d</i> ₂	<i>d</i> ₃	<i>d</i> ₄	<i>d</i> ₅	$\dot{\epsilon}_0(s^{-1})$
DP590	0.7	0.5	5	-0.006	0.0	0.02
Al5052	0.29	1.49	3.32	0.0	0.0	0.01

Table 5 The definition of the simulation parameters

Conditions	Friction coefficient	Initial temperature (°C)	Heat transfer coefficient (W (m ³ K) ⁻¹)
Parameters	0.1	20	50

Fig. 6 The deformation comparisons between experimental and numerical results: **a** the cross-sectional geometry; **b** the cross-section parameters



hardening index and temperature factor; *T_r*, *T_m* and *T* represent the reference temperature (generally room temperature), the melting point temperature of the material and the experimental temperature, respectively.

In addition, the *J-C* failure model could more accurately reflect the effects of tensile and compressive stresses during material failure compared with the equivalent effect damage criterion [26]. Its expression was:

$$\epsilon_f = [d_1 + d_2 \exp(d_3 \eta)] [1 + d_4 \ln \frac{\dot{\epsilon}}{\dot{\epsilon}_0}] [1 + d_5 \left(\frac{T - T_r}{T_m - T_r} \right)] \tag{2}$$

where ϵ_f is the effective fracture strain; η is the stress triaxiality factor; *d*₁, *d*₂, *d*₃, *d*₄ and *d*₅ represent the damage constant related to the material.

The relevant parameters of the sheets were obtained by tensile and fracture tests, as shown in Tables 3 and 4.

Referring to previous relevant research [27], the interaction was set to General contact (Explicit). Specifically, the penalty function method was used for tangential contact,

and the hard contact method was used for normal contact. The friction coefficients of all contact surfaces were set to 0.1. Furthermore, it was noticeable that the top sheet needed to add the self-contact to avoid interference between the failed mesh and the top sheet [28]. As a cold forming process, the springback of deformed rivet and sheets was involved in the riveting process. Therefore, an additional analysis step was added to analyze the spring back processes of rivet and sheets by relieving the relevant contact with the punch, blank holder and die. Table 5 shows the definition of the simulation parameters required for the model.

Figure 6a shows the comparison of cross-sectional geometry between experimental and numerical results. It could be seen that there was a slightly difference in the global cross-section, and the differences of three structure parameters were all small. Figure 6b shows the comparison of cross-section parameters. In general, the errors of these structural parameters were within 10%. So, it verified that the three-dimensional explicit FEM of the SPR joint in this study was relatively accurate.

Results and discussion

Riveting process

In order to analyze the impact of die misalignment on the riveting process, the comparisons of the riveting process for specimens No. 0, No. 5 and No. 10 were carried out, as shown in Fig. 7. It could be seen that the riveting process of SPR joints with different misalignment distance was basically the same until the rivet touched the bottom sheet. At this time, the stroke distance of punch was approximately 3 mm. For the normal riveted joint, the structural difference between the left and right ends was relatively small due to the same size of the deformation zone. For the misaligned riveted joint, the structural difference between the left and right ends gradually increased with the riveting process. Specifically, after the rivet contacted the bottom sheet, the left end of rivets could not continue to deform significantly downward and outward due to the close to the die edge, while the right end could continue to deform significantly without this limitation. When the left end of die was filled with material, the deformation resistance of the left end of rivets would increase. At this moment, the rivet leg was thickened with the riveting process.

Figure 8 shows the comparisons of cross-sectional geometry of SPR joints with different misalignment distance. It could be seen that the asymmetry of SPR joints gradually became obvious as the misalignment distance increased. Specifically, for the left end of rivets (L), the deformation was limited because the rivet leg was away from the die center and close to the die edge. This resulted in the rivet

legs unable to extend outward and down too far. At this time, the phenomenon of thick rivet legs became more obvious, and the minimum thickness of bottom sheets decreased. For the right end of rivets (R), the deformation was basically the same. There was a large space for rivet deformation because the rivet leg was away from the die edge. However, this resulted that the top sheet did not fit tightly with the bottom sheet. At the outer edge of rivet legs, a cavity was formed between the top and bottom sheet.

Stress and strain

The stress variation in rivet legs was basically the same before the stroke distance of 3 mm. It was because that the riveting process of SPR joints with different misalignment distance was basically the same until the rivet touched the bottom sheet. Therefore, only the stress variation after the stroke distance of 3 mm was analyzed. Figure 9 shows the comparison of the stress variation in rivet legs for specimens No. 0, No. 5 and No. 10. It could be seen from Fig. 9a that the principal stress at the left and right ends of rivet legs were almost the same for the normal riveted joint. For the misaligned riveted joint, the principal stress at the left end of rivet legs would change dramatically at some point as shown in Fig. 9b and c. Specifically, the change occurred at the stroke distance of 5.787 mm for SPR joints with the misalignment distance of 0.5 mm, while it occurred at the stroke distance of 4.741 mm for SPR joints with the misalignment distance of 1.0 mm. It indicated that the change would advance with increasing misalignment distance. It was because the deformation space of rivets became smaller

Fig. 7 The comparisons of riveting process

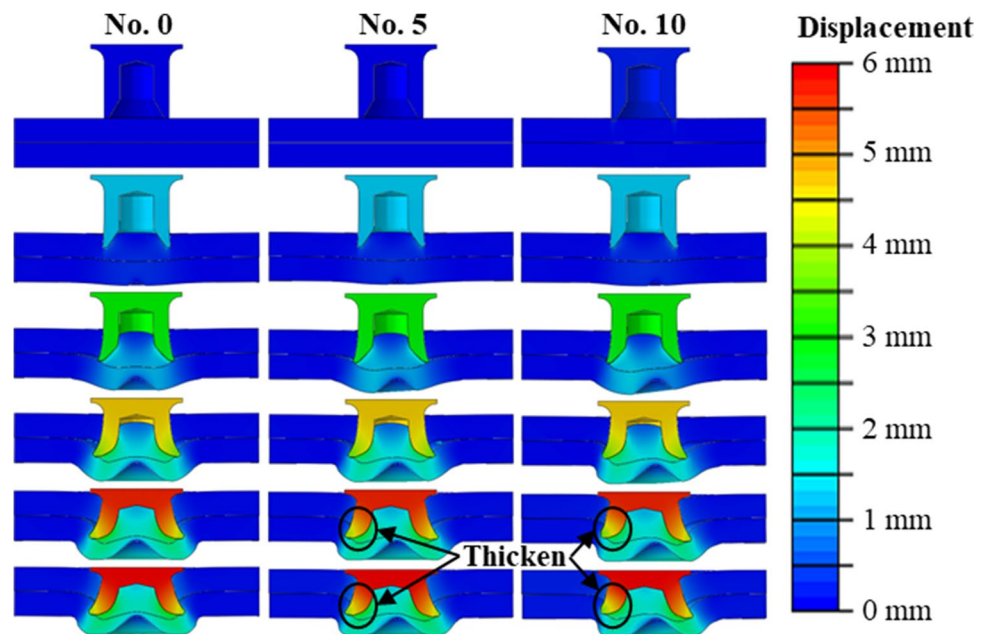
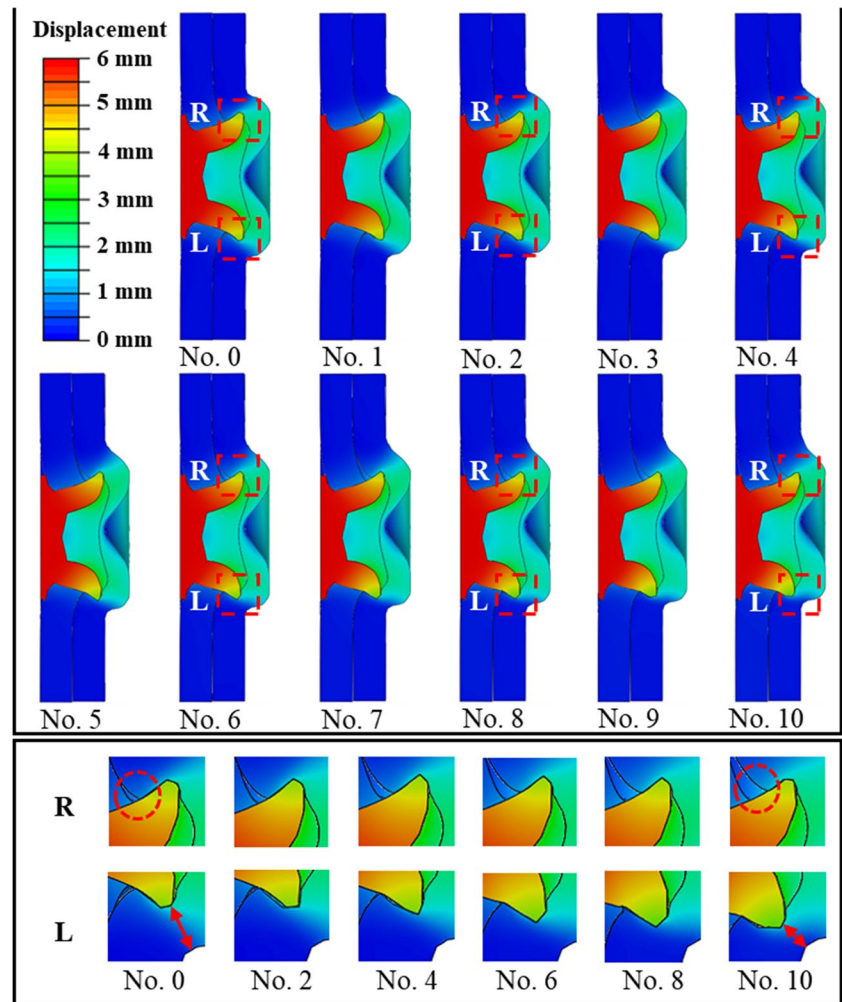


Fig. 8 The comparisons of cross-sectional geometry



and the deformation resistance increased, as the rivet legs moved closer to the die edge. At this moment, the rivet leg tip was thickened and in the tensile stress state. In addition, the principal stress at the right end of rivet legs was approximately the same as that of the normal riveted joint, basically within the range of -0.8 GPa to -0.3 GPa. Moreover, it could be seen from Fig. 9d that the maximum stress difference between the left and right ends of rivet legs also increased as the misalignment distance increased.

Figure 10 shows the plastic strain distribution map of rivet after riveting process for SPR joints with different misalignment distance. In order to provide a better view of the main strain form on the rivet legs, they were displayed outward. Positive values represented tensile deformation (marked in red), and negative values represented compressive deformation (marked in blue). It could be seen that there were red rings around all the rivet legs. It was because the rivet legs would expand outward and generate tensile strain during the riveting process. For the normal riveted joint, the strain distribution on the left and right sides of rivet legs were basically consistent. This indicated that the deformation of the

rivet leg tip was relatively balanced. Specifically, the rivet leg tip exhibited tensile strain, while its left and right sides exhibited compressive strain. This was because the rivet leg tips became thicker, and its left and right sides were subject to deformation resistance from the sheets during the riveting process. For the misaligned riveted joint, there was a difference in the strain distribution on the left and right sides of rivet legs, and it became significant as the misalignment distance increased. The left rivet leg tip exhibited tensile strain, while the right side mainly exhibited smaller compressive strain. It was because the left end of rivet legs was close to the die edge, and the deformation was limited. At this time, the deformation resistance was increased and the phenomenon of thick rivet legs became more obvious. However, the right end of rivet legs had plenty of deformation space due to being away from the die edge, and the deformation resistance was decreased.

Figure 11 shows equivalent plastic strain distribution of bottom sheet after riveting process for SPR joints with different misalignment distance. For the lower surface of bottom sheet contacting with the die edge, the strain increased on the left side and decreased on the right side with the

Fig. 9 The stress variation in rivet legs: **a** specimen No. 0; **b** specimen No. 5; **c** specimen No. 10; **d** the maximum stress difference

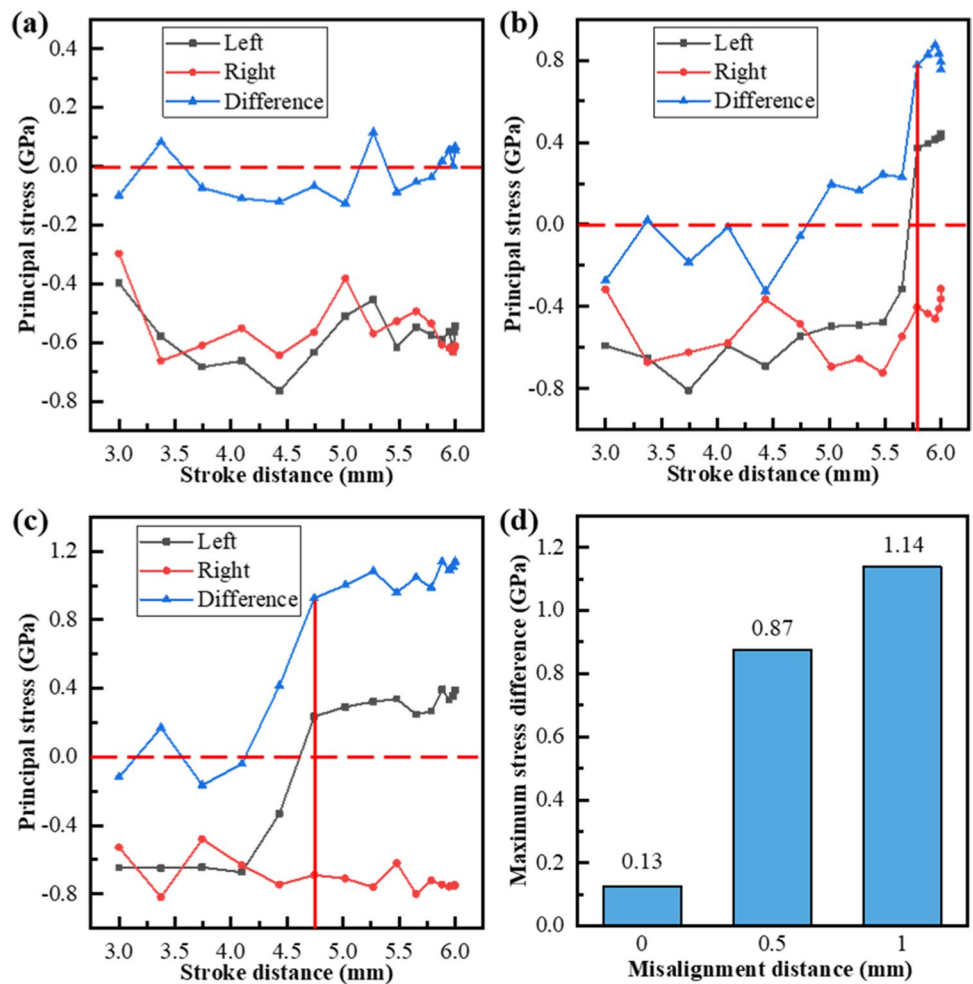
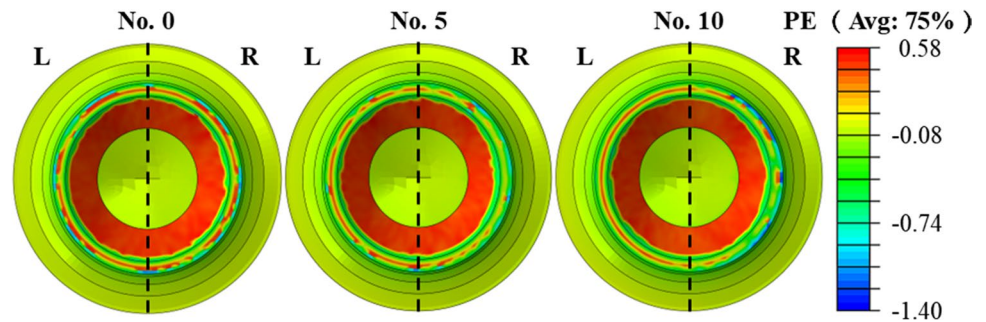


Fig. 10 The plastic strain distribution map of rivet after riveting process



increase of the misalignment distance. For the lower surface of bottom sheet contacting with the central bulge of the die, the maximum equivalent plastic strain increased and the zone of maximum strain was gradually shifted to the right side as the misalignment distance increased. In addition, it could be seen from the cross-sectional geometry that there was a uniform annular deformation zone in the normal riveted joint. However, for the misaligned riveted joint, the deformation zone on the left side became significantly wide, while that on the right side became narrower. This phenomenon became more apparent with increasing misalignment

distance. This was because the extrusion force from the rivet and die became greater for the left deformation zone, and it was less for the right deformation zone.

Cross-section parameters

To further investigate the expansion of rivets in the sheets, the horizontal and vertical displacements of rivet legs of SPR joints with different misalignment distance were obtained, as shown in Fig. 12. It could be seen that the horizontal and vertical displacements did not significantly change for the

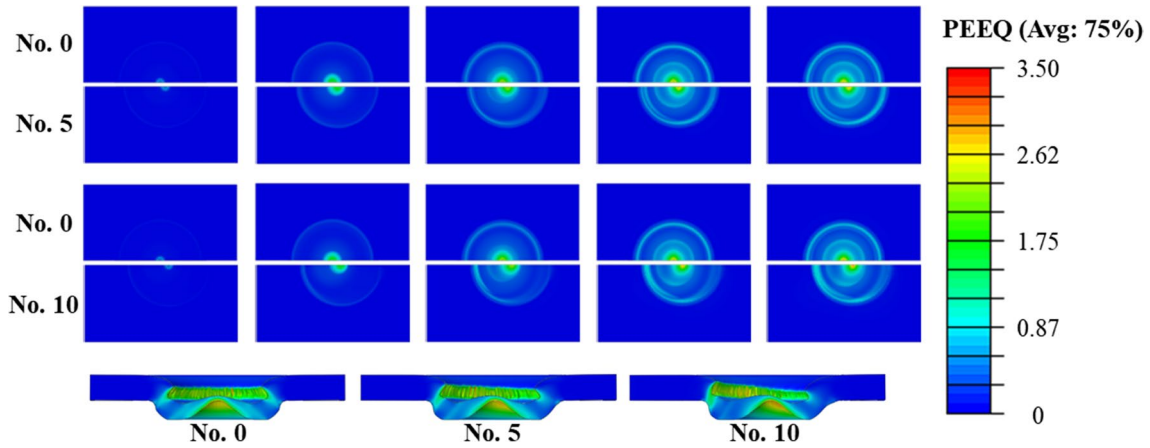


Fig. 11 The equivalent plastic strain distribution of bottom sheet after riveting process

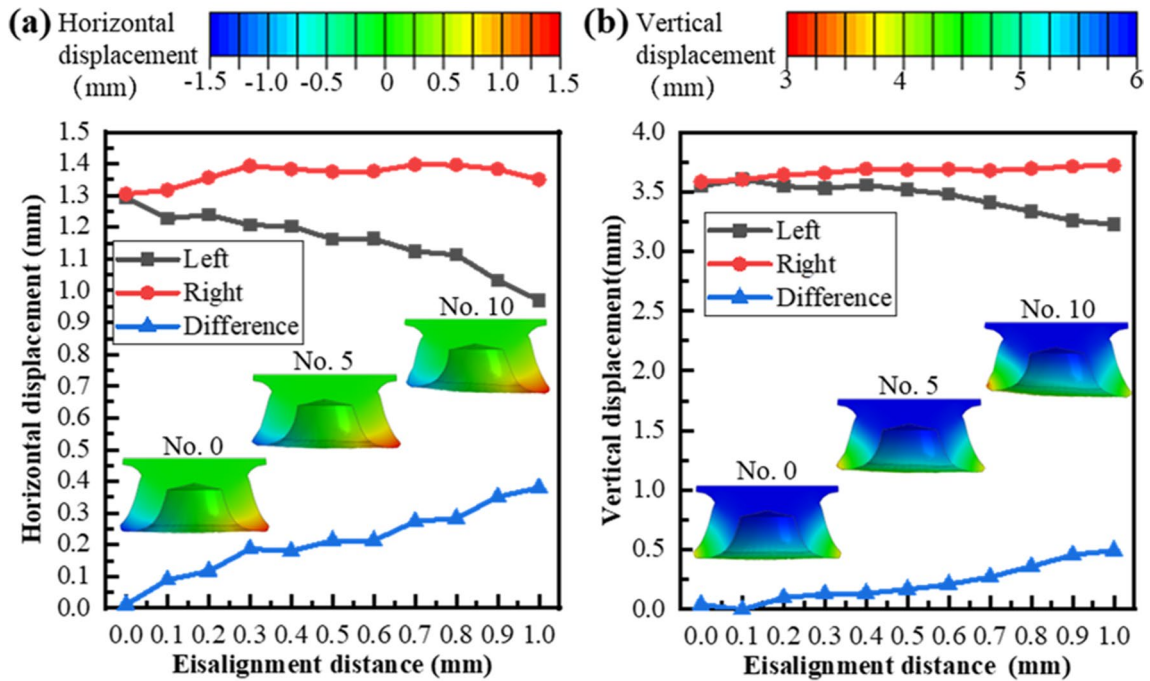
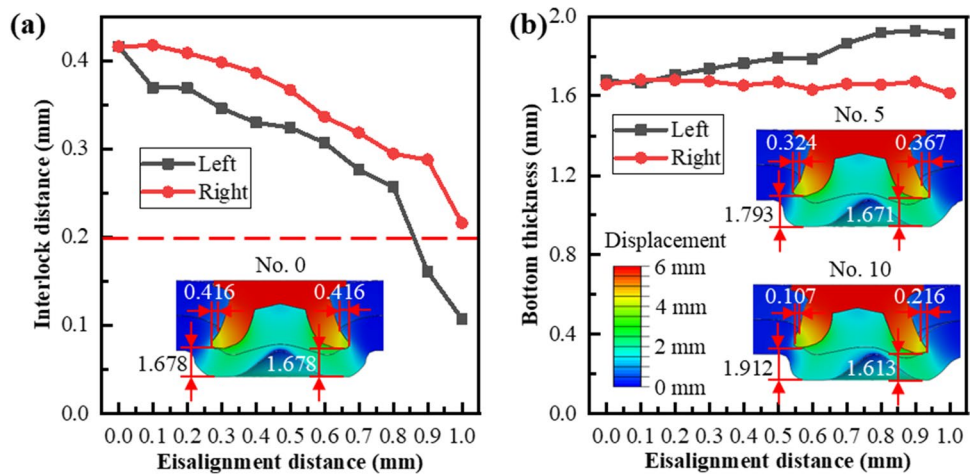


Fig. 12 The displacement of rivet legs: **a** the horizontal displacement; **b** the vertical displacement

right end of rivet legs, while both decreased significantly for the left end of rivet legs, as the misalignment distance increased. Specifically, for the right end of rivet legs, both horizontal and vertical displacements increased slightly with the increase of misalignment distance. This was because the deformation resistance of rivets was decreased as the rivet legs were away from the die edge. On the contrary, for the left end of rivet legs, the deformation resistance was increased as the rivet legs were close to the die edge. This resulted that it was difficult for the left end of rivet legs to expand in the sheets, and both horizontal and vertical displacements were significantly reduced.

In this study, the stroke distance was both set to 6 mm, and the residual height of rivet head was basically in the range of 0.05–0.1 mm after riveting process. Therefore, only the other two parameters were analyzed. Figure 13 shows the comparisons of cross-section parameters of SPR joints with different misalignment distance. It could be seen from Fig. 13a that the interlock distance decreased as the misalignment distance increased for both the left and right ends of rivets. However, the reasons for these phenomena were different. For the left end of rivet legs, it was due to the decreasing deformation space with increasing dislocation distance, resulting in the inability of the rivet leg to expand

Fig. 13 The comparisons of cross-section parameters: **a** the interlock distance; **b** the bottom thickness



outward. For the right end of rivet legs, it was because the deformation space became large as the misalignment distance increased. This caused that the top and bottom sheets do not fit tightly together, and a cavity was formed between the rivet legs and sheets. In addition, previous studies showed that qualified SPR joints had interlock distances greater than 0.2 mm [29]. The interlock distance was less than 0.2 mm with the misalignment distance of the left end of rivets not less than 0.9 mm, while it was all greater than 0.2 mm with the misalignment distance of the right end of rivets less than 1.0 mm. Moreover, the bottom thickness increased with the increase of the misalignment distance for the left ends of rivets, as shown in Fig. 13b. This was because, during the riveting process, the deformation resistance of the left end of rivets increased due to being close to the die edge. At the same time, the rivet legs were thickened, thereby reducing the puncture of the bottom sheet. However, the bottom thickness decreased slightly with increasing misalignment distance for the right end of rivets. It was because the deformation space of rivet legs became large, leading to downward expansion of rivet legs.

Mechanical properties degradation

The die misalignment caused the change in the cross-section parameters of SPR joints, and this would lead to the variation of mechanical properties [22]. Therefore, the effect of die misalignment on the mechanical properties of SPR joints was further investigated. Figure 14 depicts the shear load–displacement curves of SPR joints with different misalignment distance. Among them, the offset distance of the die towards the fixed end indicated a positive offset, while the offset distance of the die towards the loading end represented a negative offset. It could be seen that the curves almost coincided in the elastic deformation stage, and the curve trends were still the same in the plastic deformation stage. For the normal riveted joint, the shear load increased

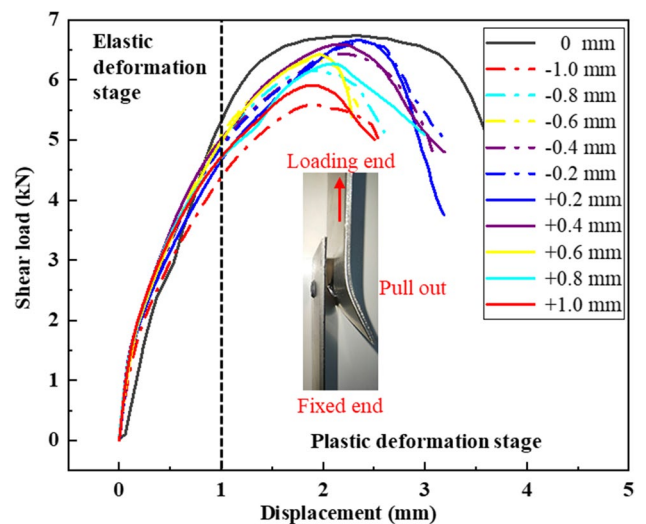
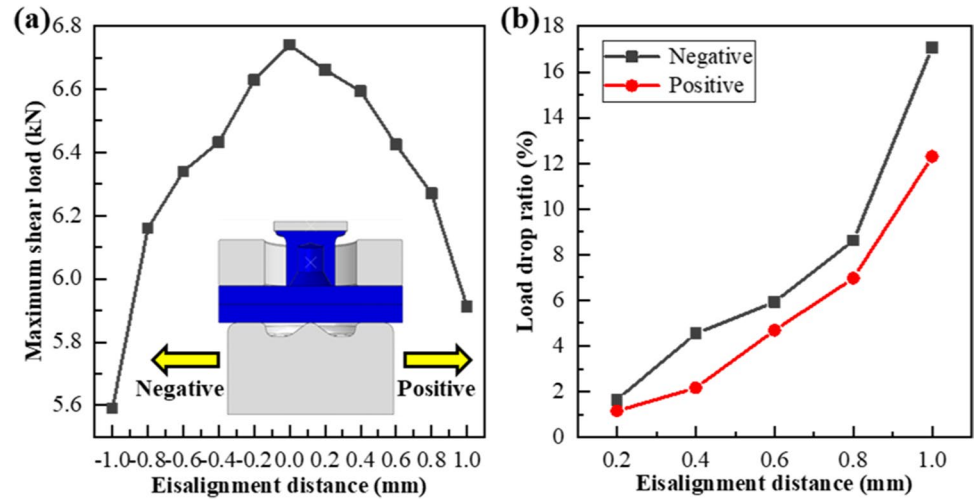


Fig. 14 The shear load–displacement curves of SPR joints with different misalignment distance

gradually and then decreased, and the shear load reached the maximum when the displacement was about 2.5 mm. For the misaligned riveted joint, the peak load and failure displacement decreased with the increase of misalignment distance. There were some differences in the effect of both SPR joints with equivalent misalignment distance on the maximum shear, and the differences decreased as the misalignment distance increased. In addition, during shear loading, the failure mode of SPR joints was that the rivet was pulled out from the bottom sheet near the fixed end, resulting in the failure of the interlocking structure.

To intuitively observed, Fig. 15a shows the maximum shear load of SPR joints with different misalignment distance. It could be seen that the maximum shear load decreased for both SPR joints with positive and negative misalignment distance, and the degree of decrease was different. Therefore, the degradation law of mechanical

Fig. 15 The mechanical properties degradation: **a** the maximum shear load; **b** the load drop ratio



properties of SPR joints with different misalignment distance was obtained. Based on Eq. (3), the load drop ratio of SPR joints with different misalignment distance was obtained [30], as shown in Fig. 15b. It could be seen that the effect on the maximum shear load of shifting along the negative direction was significantly greater than that of shifting along the positive direction. That was because the interlock distance near the fixed end with negative misalignment distance would be greater than that with the same positive misalignment distance. In addition, the maximum shear load did not decrease linearly as misalignment distance increased.

This was mainly because the interlock distance of SPR joints decreased nonlinearly due to the die misalignment, as shown in Fig. 13a.

$$LDR = (L_0 - L_X)/L_0 \tag{3}$$

where LDR is the load drop ratio of SPR joints, L_0 is the maximum shear load of the normal riveted joint and L_X is the maximum shear load of joints with the misalignment distance of X mm.

Figure 16 shows the shear failure of SPR joints with different misalignment distance. It could be seen that the shear

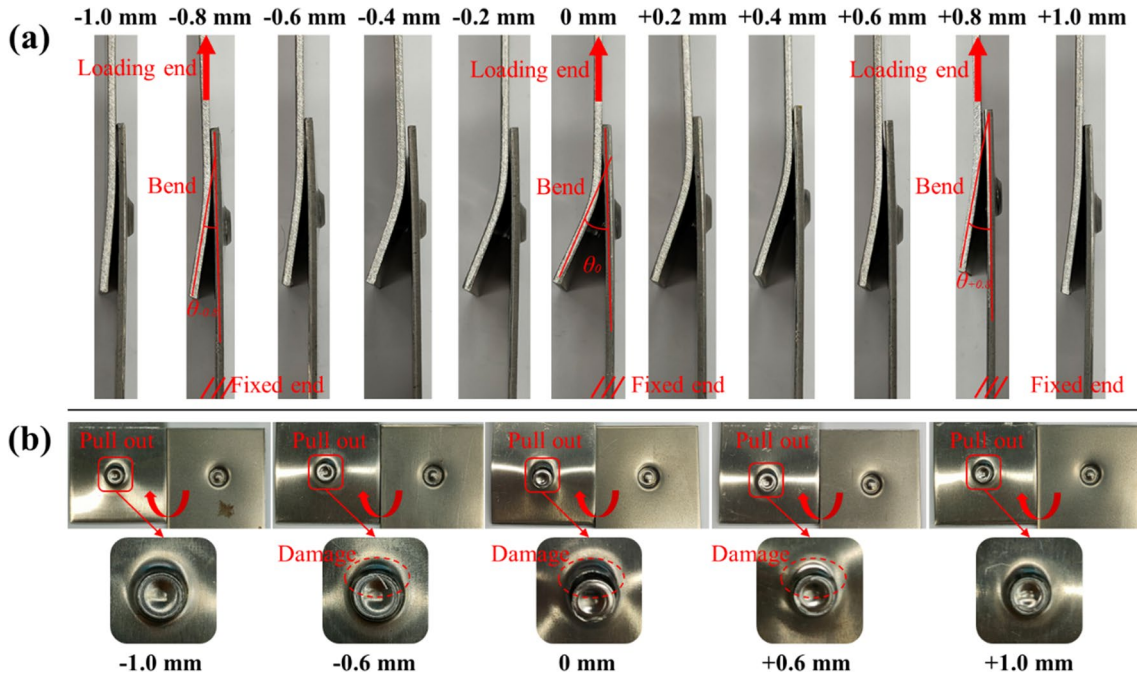


Fig. 16 The shear failure of SPR joints with different misalignment distance: **a** the failure state; **b** the failure appearance

failure modes of SPR joints were all the damage of interlocking structure. Specifically, the rivet together with the Al sheet was pulled out from the steel sheet near the fixed end. In addition, it could be seen from Fig. 16a that the bending degrees of Al sheet decreased with increasing misalignment distance. The damage degree of Al sheet near the loading end also decreased as the misalignment distance increased, as shown in Fig. 16b. It was because the interlock distance of SPR joints decreased with the increase of misalignment distance, resulting in a decrease in peak load and failure displacement.

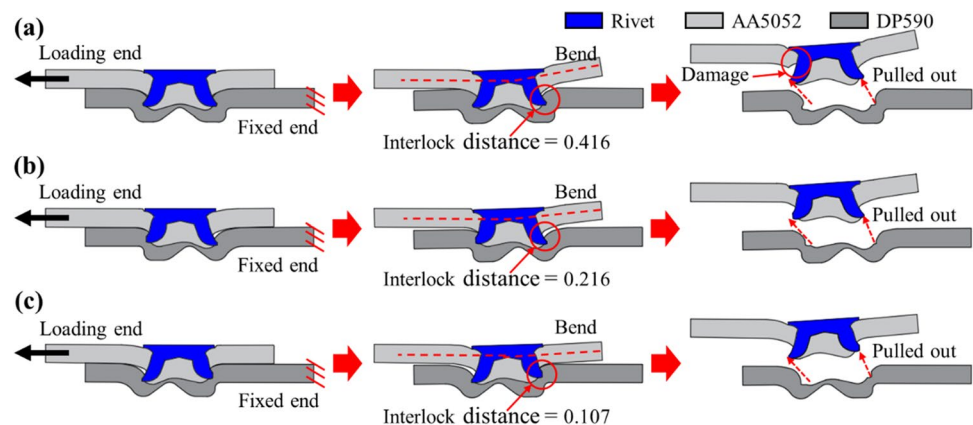
Based on the above results, the mechanical properties degradation mechanism of the misaligned riveted joints was analyzed. For the normal riveted joint (the misalignment distance of 0 mm), as shown in Fig. 17a, the torque generated at the lap zone led to the deflection of rivets due to the asymmetric structure of specimens, during the shearing process [5]. The Al sheet near the fixed end gradually bent with the increase of shear load. Then the interlocking structure between rivet and sheets was destroyed near the fixed end. Finally, the rivet together with the Al sheet was pulled out from the steel sheet. For the misaligned riveted joints, the failure process and failure mode were basically consistent with the above, as shown in Fig. 17b and c. However, there was a certain difference in the damages of interlocking structures due to the different cross-section parameters. Specifically, when the die was shifted toward the fixed end, a cavity was formed between the rivet leg and bottom sheets, and the interlock distance and bottom thickness near the fixed end decreased slightly. However, when the mold was shifted toward the loading end, the rivet leg was thickened due to limitations in deformation space. The interlock distance decreased sharply and bottom thickness increased slightly at the fixed end. The interlock distance of SPR joints was asymmetrically and nonlinearly reduced due to the die misalignment. It resulted in different maximum shear loads of SPR joints and bending degrees of Al sheet, as shown in Figs. 15a and 16a, respectively.

Conclusions

In this paper, the influence of die misalignment on the cross-section parameters and mechanical properties of SPR joints were respectively investigated through numerical simulation and experiment. Based on the above results and analysis, the following conclusions could be drawn:

1. For the misaligned riveted joint, the rivet leg near the die edge was thickened with the riveting process due to limitations in deformation space. At the outer edge of the rivet leg near the die center, a cavity was formed between the top and bottom sheet.
2. The principal stress in the rivet leg near the die edge would change from compressive stress to tensile stress at some point, and the change would increase with increasing misalignment distance. It was because the deformation space of rivets became smaller and the deformation resistance increased, as the rivet legs moved closer to the die edge.
3. The principal stress in the rivet leg near the die center was approximately the same as that of the normal riveted joint. It was because it had plenty of deformation space, and the deformation resistance was decreased due to being away from the die edge.
4. For the misaligned riveted joint, the interlock distance decreased as the misalignment distance increased. The bottom thickness of the side near the die edge increased with the increase of misalignment distance, while that near the die center decreased slightly with increasing misalignment distance.
5. Compared with the normal riveted joint, the maximum shear load of the misaligned riveted joint decreased. The movement of the die along the loading end had a significantly greater impact on the maximum shear load than the movement along the fixed end. In addition, the maximum shear load did not decrease linearly with increasing misalignment distance. This was mainly because the interlock distance of SPR joints decreased nonlinearly due to the die misalignment.

Fig. 17 The schematic of mechanical properties degradation mechanism: **a** the normal riveted joint; **b** the positive eccentric riveted joint; **c** the negative eccentric riveted joint



Acknowledgements This project was supported by the National Natural Science Foundation of China (Nos. 52005173 and 52375331), and the Shenzhen Science and Technology Program (KQTD20200820113110016).

Data availability The raw/processed data required to reproduce these findings cannot be shared at this time due to technical or time limitations.

Declarations

Conflict of interest None.

References

- Busse S, Merklein M, Roll K et al (2010) Development of a mechanical joining process for automotive body-in-white production. *Int J Mater Form* 3:1059–1062. <https://doi.org/10.1007/s12289-010-0953-3>
- Liao Y, Sun H, Wu G et al (2023) Effect of rivet arrangement on fatigue performance of electromagnetic riveted joint with $\Phi 10$ mm diameter rivet. *Int J Fatigue* 107892. <https://doi.org/10.1016/j.ijfatigue.2023.107892>
- Di Franco G, Fratini L, Pasta A, Ruisi VF (2013) On the self-piercing riveting of aluminium blanks and carbon fibre composite panels. *Int J Mater Form* 6:137–144. <https://doi.org/10.1007/s12289-011-1067>
- Rusia A, Weihe S (2020) Development of an end-to-end simulation process chain for prediction of self-piercing riveting joint geometry and strength. *J Manuf Process* 57:519–532. <https://doi.org/10.1016/j.jmapro.2020.07.004>
- Jiang H, Liao Y, Gao S et al (2021) Comparative study on joining quality of electromagnetic driven self-piercing riveting, adhesive and hybrid joints for Al/steel structure. *Thin-Walled Struct* 164:107903. <https://doi.org/10.1016/j.tws.2021.107903>
- Han L, Thornton M, Shergold M (2010) A comparison of the mechanical behaviour of self-piercing riveted and resistance spot welded aluminium sheets for the automotive industry. *Mater Design* 31:1457–1467. <https://doi.org/10.1016/j.matdes.2009.08.031>
- Asati B, Shajan N, Akhil Kishore VT et al (2022) A comparative investigation on self-piercing riveting and resistance spot welding of automotive grade dissimilar galvanized steel sheets. *Int J Adv Manuf Technol* 123:1079–1097. <https://doi.org/10.1007/s00170-022-10226-y>
- Deng J-H, Lyu F, Chen R-M, Fan Z-S (2019) Influence of die geometry on self-piercing riveting of aluminum alloy AA6061-T6 to mild steel SPFC340 sheets. *Adv Manuf* 7:209–220. <https://doi.org/10.1007/s40436-019-00250-9>
- Karathanasopoulos N, Pandya KS, Mohr D (2021) An experimental and numerical investigation of the role of rivet and die design on the self-piercing riveting joint characteristics of aluminum and steel sheets. *J Manuf Process* 69:290–302. <https://doi.org/10.1016/j.jmapro.2021.07.049>
- Jiang H, Gao S, Li G, Cui J (2019) Structural design of half hollow rivet for electromagnetic self-piercing riveting process of dissimilar materials. *Mater Design* 183:108141. <https://doi.org/10.1016/j.matdes.2019.108141>
- Karim MA, Jeong T-E, Noh W et al (2020) Joint quality of self-piercing riveting (SPR) and mechanical behavior under the frictional effect of various rivet coatings. *J Manuf Process* 58:466–477. <https://doi.org/10.1016/j.jmapro.2020.08.038>
- Duan J, Chen C (2023) Effect of edge riveting on the failure mechanism and mechanical properties of self-piercing riveted aluminium joints. *Eng Fail Anal* 150:107305. <https://doi.org/10.1016/j.engfailanal.2023.107305>
- Chen G, Zeng K, Xing B, He X (2022) Multiple nonlinear regression prediction model for process parameters of Al alloy self-piercing riveting. *J Mater Res Technol* 19:1934–1943. <https://doi.org/10.1016/j.jmrt.2022.05.118>
- Pan M, Tang W, Xing Y, Ni J (2018) Numerical simulation analysis for deformation deviation and experimental verification for an antenna thin-wall parts considering riveting assembly with finite element method. *J Cent South Univ* 25:60–77. <https://doi.org/10.1007/s11771-018-3717-8>
- Du Z, Duan L, Jing L et al (2021) Numerical simulation and parametric study on self-piercing riveting process of aluminium–steel hybrid sheets. *Thin-Walled Struct* 164:107872. <https://doi.org/10.1016/j.tws.2021.107872>
- Zhao H, Han L, Liu Y, Liu X (2022) Analysis of joint formation mechanisms for self-piercing riveting (SPR) process with varying joining parameters. *J Manuf Process* 73:668–685. <https://doi.org/10.1016/j.jmapro.2021.11.038>
- Lin J, Qi C, Wan H et al (2021) Prediction of cross-tension strength of self-piercing riveted joints using finite element Simulation and XGBoost Algorithm. *Chin J Mech Eng* 34:36. <https://doi.org/10.1186/s10033-021-00551-w>
- Ang HQ (2021) An overview of self-piercing riveting process with focus on joint failures, corrosion issues and optimisation techniques. *Chin J Mech Eng* 34:2. <https://doi.org/10.1186/s10033-020-00526-3>
- Chung C-S, Kim H-K (2016) Fatigue strength of self-piercing riveted joints in lap-shear specimens of aluminium and steel sheets: fatigue. *Fatigue Fract Engng Mater Struct* 39:1105–1114. <https://doi.org/10.1111/ffe.12419>
- Afonso RM, Alves LM (2023) Double-sided self-pierce riveting: rivet geometry optimization. *Int J Mater Form* 16:34. <https://doi.org/10.1007/s12289-023-01760-5>
- Haque R (2018) Quality of self-piercing riveting (SPR) joints from cross-sectional perspective: a review. *Arch Civ Mech Eng* 18:83–93. <https://doi.org/10.1016/j.acme.2017.06.003>
- Asati B, Shajan N, Singh Arora K (2022) Effect of process parameters on joint performance in self-piercing riveted dissimilar automotive steel joints. *Mater Today: Proc* 62:721–726. <https://doi.org/10.1016/j.matpr.2022.03.658>
- Jessadatavornwong P, Huff G, Freis A et al (2023) Characterization of self-piercing rivet joints using X-ray computed tomography. *Tomography Mater Struct* 100010. <https://doi.org/10.1016/j.tmater.2023.100010>
- Liao Y, Zhong J, Li G et al (2022) Influence of adhesive on dynamic performance of steel/Al electromagnetic clinched joints. *Archiv Civ Mech Eng* 22:177. <https://doi.org/10.1007/s43452-022-00504-7>
- Paik JK, Kim KJ, Lee JH et al (2017) Test database of the mechanical properties of mild, high-tensile and stainless steel and aluminium alloy associated with cold temperatures and strain rates. *Ships Offshore Struct* 12:S230–S256. <https://doi.org/10.1080/17445302.2016.1262729>
- Xu H, Zhang Y, Peng R et al (2021) Simulation and experimental study on the strength of Al7075-T6 clinched joint. *Eng Fail Anal* 129:105735. <https://doi.org/10.1016/j.engfailanal.2021.105735>
- Fang Y, Huang L, Zhan Z, Huang S, Liu X, Chen Q, Zhao H, Han W (2022) A framework for calibration of self-piercing riveting process simulation model. *J Manuf Process* 76:223–235. <https://doi.org/10.1016/j.jmapro.2022.01.015>

28. Wang J, Zhang G, Zheng X et al (2021) A self-piercing riveting method for joining of continuous carbon fiber reinforced composite and aluminum alloy sheets. *Compos Struct* 259:113219. <https://doi.org/10.1016/j.comstruct.2020.113219>
29. Karim MA, Murugan SP, Bae K et al (2022) Effect of top sheet materials on joint performance of self-piercing riveting. *J Weld Join* 40:512–524. <https://doi.org/10.5781/JWJ.2022.40.6.7>
30. Jiang H, Liao Y, Jing L et al (2021) Mechanical properties and corrosion behavior of galvanized steel/Al dissimilar joints. *Archiv Civ Mech Eng* 21:168. <https://doi.org/10.1007/s43452-021-00320-5>

Publisher's Note Springer Nature remains neutral with regard to jurisdictional claims in published maps and institutional affiliations.

Springer Nature or its licensor (e.g. a society or other partner) holds exclusive rights to this article under a publishing agreement with the author(s) or other rightsholder(s); author self-archiving of the accepted manuscript version of this article is solely governed by the terms of such publishing agreement and applicable law.